Diamond NV centers based quantum sensor using a VCO integrated with filtering antenna

Gao, Yang; Zeng, Yong; Cui, Mingming; Qiao, Yingying; Yang, Xun; Lin, Chaonan; Zhao, Jiale; Li, Lei; Wang, Yi; Shan, Chongxin

Link to publication on Research at Birmingham portal

Diamond NV Centers based Quantum Sensor using a VCO Integrated with Filtering Antenna

Yang Gao, *IEEE*, *Member*, Yong Zeng, Mingming Cui, Yingying Qiao, Xun Yang, Chaonan Lin, Jiale Zhao, Lei Li, Yi Wang, *IEEE*, *Senior Member* and Chongxin Shan

Abstract—**This paper presents a diamond nitrogen-vacancy (NV) center based magnetic field sensor using a voltage-controlled oscillator (VCO) integrated with a filtering antenna. In existing NV-based quantum sensing systems, microwave source and delivery units are implemented by a set of bulky and costly instruments. This limits its practical applications as well as portability. Here, a VCO integrated with the filtering antenna is designed, providing a more uniform, efficient, broadband and lower phase noise microwave field coupling to the NV centers. As a result, the sensitivity and the dynamic range have been improved over the conventional scheme using separate microwave components, such as antennas, transmission lines, and resonators. Moreover, in this work, the optic filter, and photodetector are also integrated using the hybrid microwave integrated circuits (HMIC) technique for the first time. This significantly increases the integration level and reduces the cost of the NV-based magnetometers. The experimental results indicate that our VCO integrated filtering antenna achieves a sensitivity of 8.52 μT/Hz$^{1/2}$ and a dynamic range up to <mark>32.73 dB</mark>, which are both greatly improved compared to the VCO with a single resonator. This validates the effectiveness of the approach.**

Index Terms—**Diamond NV centers, quantum sensor, spin-state, microwave integrated circuits, GaAs transistor oscillator.**

I. INTRODUCTION

MAGNETIC field sensing and measurements have been widely used in engineering and scientific research, such as resource exploration, industrial detection, navigations, biomedical sciences, etc [1]-[5]. Recently, magnetic field metrologies based on quantum techniques have got much attention for their non-destructive testability, high sensitivity, and stability in extreme environments. Among the quantum systems, the NV centers in diamond become a distinct candidate because of their long-spin coherence time, initialized and manipulable spin-state, and optical readout at room temperature [6]-[10]. The NV center's excellent physical properties allow for the in-situ, non-invasive, high-precision magnetic field, measurement and sensing [11]-[18]. Furthermore, NV-based magnetic sensing, combined with scanning imaging techniques, can achieve magnetic imaging with ultra-high resolution. Latest applications have been extended to microwave fields, such as failure diagnosis of
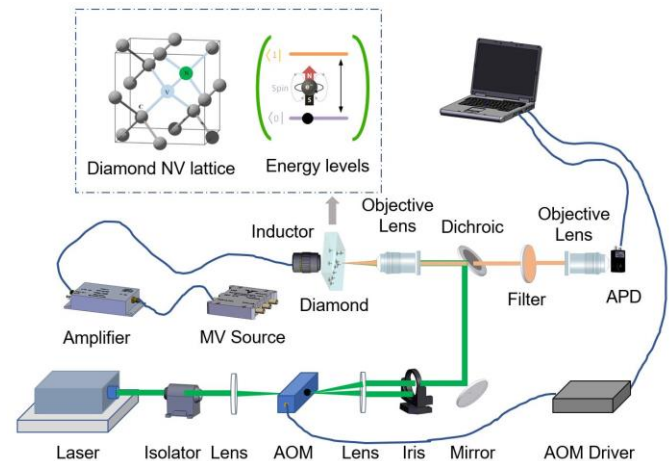
Fig. 1 The schematic of the NV-based magnetic field sensing technique. After modulated with an AOM (acoustic optical modulator), the 532 nm light is injected into a diamond, causing it to fluoresce. The fluorescence is separated from the green light by a dichroic plate. Then the fluorescence is further purified by a filter and detected by a photon detector. The computer is used to control the AOM and to obtain the qubit readout. The figure in the upper left corner refers to NV-based quantum sensor system (qubit resonance of the NV in diamond).

microwave integrated circuit (IC) [19]-[21], near field imaging of antenna [22], and broadband radio frequency (RF) field imaging [23].

For NV-based magnetic field sensing techniques, the optically detected magnetic resonance (ODMR) technique is widely applied [24], [25]. By receiving optically detected fluorescence, which results from the electron spin transition, the qubit resonance of NV centers can be obtained. This diamond NV-based quantum sensing system consists of specific microwave and photoelectric instruments. As illustrated in Fig. 1, the microwave source and amplifier are used to drive the NV electron spin; avalanche photodiode detector is employed for NV spin-dependent fluorescence measurements; the optical filter is to select the fluorescence of the diamond and reject green light from the laser; and a 532 nm green pump laser is also required for qubit initialization.

In conventional quantum magnetometers, these microwave

Fig. 2 (a) Lattice structure of the NV center in diamond and the diamond sample. (b) The ODMR fluorescence spectrum. (c) The energy level diagram of the NV center. The ground state $^3A_2$ has a spin-triplet with a zero-field splitting D_{gs} = 2.87 GHz between the $|0\rangle$ and $|\pm 1\rangle$ states. The $|\pm 1\rangle$ states split due to the external magnetic field which is proportional to the B_0 along the NV symmetry axis. (d) Diagram of the diamond NV center-based sensor.
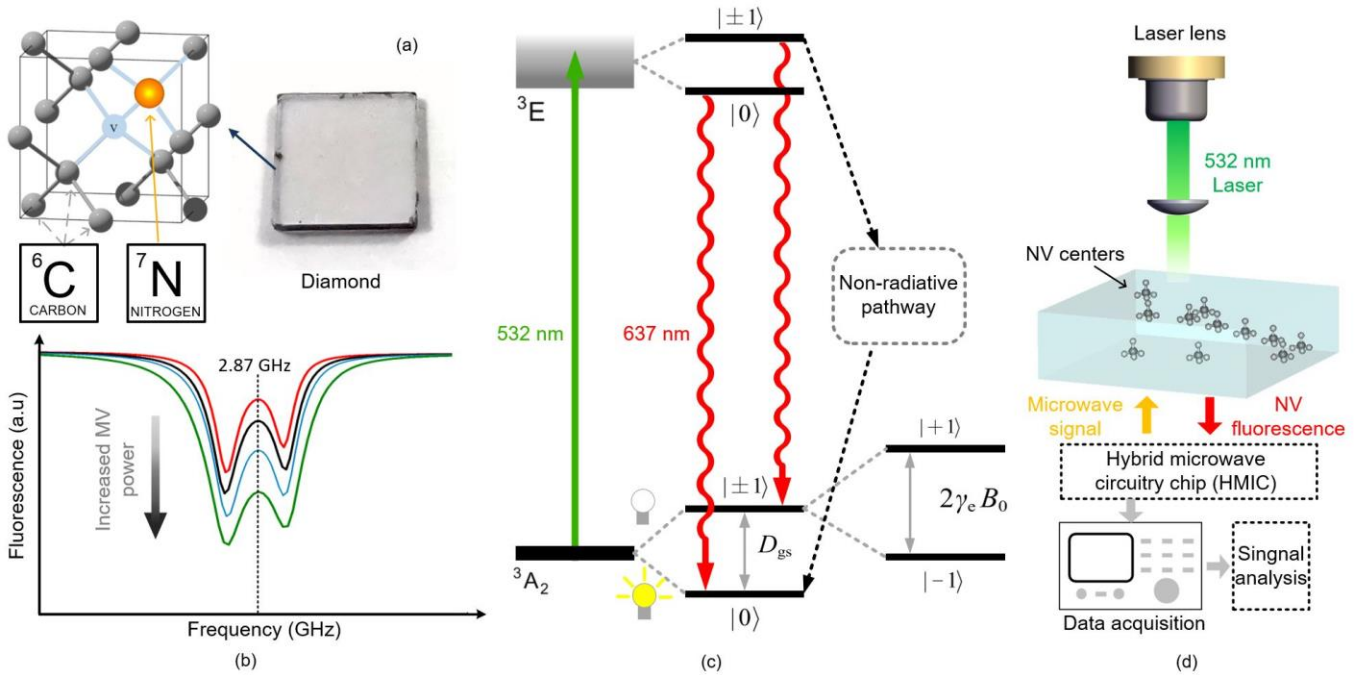
and optical units involve discrete instruments and components [19]-[23], which makes the system bulky and costly. These independent units limit the practical applications as well as portability and flexibility in usage. Moreover, in general, NV-based sensing systems, the microwave delivery techniques usually apply individual transmission lines [26], loop antenna [27], ring resonators [28], or coplanar waveguide [29]. These components address NV centers with narrow bandwidth, ununiform sensing range and low-efficiency power transfer, which leads to improved sensitivity and limited dynamic range.

Recently, some studies ([24] and [25]) have developed microwave integrated circuits (ICs) for the NV-based sensor, by integrating VCO and photodiode using the complementary metal-oxide semiconductor (CMOS) technique. This makes a great step forward for the practical use of the NV-based quantum sensors. However, some other techniques at the circuit and device level, such as III-V semiconductor devices or hybrid printed circuits, have not been reported. Compared to CMOS, GaAs or GaN devices present ultra-low noise and higher saturation power, which can achieve better performance of the devices. Moreover, some other types of circuits, such as microstrip, can significantly reduce the cost of the NV-based magnetometer for a modest production.

The contributions of this work are as follows. (i) For the first time, the GaAs HEMT with microstrip circuit is designed, which achieves functionalities of microwave sweeping, transmitting, optical filtering, photon detection and amplification, simultaneously. Due to the good noise and power performance of the GaAs HEMT and circuits, a lower phase noise microwave signal can be obtained, which removes the need for the complex off-chip phase-locked-loop (PPL) circuits. (ii) At the circuit level, instead of using single resonators or loop

antennas [26]-[29], the microwave delivery part is replaced by a filtering antenna that is integrated with the VCO. This new design feature device increases the power transfer efficiency and the bandwidth, which leads to an improved magnetic field sensitivity and dynamic range. the filtering elements, formed of multiple resonators, can improve the oscillator's phase noise performance, which further reduces the system noise. (iii) The developed component features reduced circuit complexity, lower manufacturing cost, and easy integration with optic components, which is of great potential for practical applications. The technique is general and can be applied in other NV-based sensing or measuring systems, such as thermal, tress, electric sensors, etc.

This paper is organized as follows. Section II introduces the magnetic field sensing system using diamond NV centers. Section III describes the physical design of the microwave circuits and the ODMR detection. In Section IV, the experiment is performed, followed by the analysis and discussion of measured results. Conclusions are in Section V, together with a discussion about the limitation and future development.

II. THE NV-BASED QUANTUM SENSING SYSTEM

A. NV-based Quantum Sensor using HMIC Technique

NV center is a lattice defect in diamond, where a nitrogen atom and an adjacent vacancy substitute the two original carbon atoms. The lattice structure and the picture of a fabricated sample in our laboratory are shown in Fig. 2(a).

A specific physical property of the NV center, namely the Zeeman effect, can be used in measuring the magnetic fields with high sensitivity. Under an external static magnetic field B, Zeeman-effect measurements as a function of microwave

frequency can be obtained through the ODMR spin-dependent fluorescence. The typical spectrum is shown in Fig. 2(b) and its operation principle is discussed as follows.

As shown in the energy diagram of Fig. 2(c), the ground state of the NV center is a spin-triplet: containing $|m_s = 0, \pm1\rangle$: a $m_s = 0$ state and a degenerate $m_s = \pm1$ state. Electron spin resonance (ESR) can be used to manipulate the NV spin state between $m_s = 0$ and $m_s = \pm1$ under a given magnetic field. When no magnetic field is applied, there is only one resonance at 2.87 GHz (room temperature) corresponding to the ground-state $|0\rangle \leftrightarrow |\pm1\rangle$ transition. When a static magnetic field $\boldsymbol{B}$ is applied along an arbitrary direction, the degenerate $m_s = \pm1$ state splits into two. So does the ESR spectrum. Two resonances occur: one for the ground-state $|0\rangle \leftrightarrow |-1\rangle$ transition and the other for the ground-state $|0\rangle \leftrightarrow |+1\rangle$ transition. The spin transition frequency $v_\pm$ is determined by

$$v_\pm = (D_{gs} - \beta_T \Delta T) \pm \gamma_e B_z \tag{1}$$

where B_z is the component of $\boldsymbol{B}$ in the NV symmetry axis direction; $D_{gs} = 2.87$ GHz is the room-temperature natural ground-state splitting between $|0\rangle$ and $|\pm1\rangle$, γ_e is the electronic gyromagnetic ratio (28 GHz·T^{-1}), $\beta_T = 74$ kHz·K^{-1} and ΔT is the temperature shift from room temperature. The measurement of $v_\pm$ gives B_z and ΔT in their difference and sum, respectively. Also, measuring B_z for at least three of the four possible NV orientations in diamond quantifies all components of $\boldsymbol{B}$ for vector magnetometry.

The spin states can be read out through the fluorescence properties of the diamond NV centers. Using a 532 nm wavelength laser, the diamond NV centers can be optically pumped from $^3A_2$ ground state to ^3E excited state. Sequentially, the ^3E state can decay to $^3A_2$ state forming a cycling transition, when it emits red fluorescence. Specifically, there are two paths from the excited state to the ground state: a bright transition with red fluorescence and a dark transition without fluorescence. The spin state $m_s = 0$ undergoes a bright transition. On the contrary, the spin state $m_s = \pm1$ performs a dark transition, which it undergoes crossing into a metastable, dark spin-singlet state, and finally falls back to the $|0\rangle$ state. This leads to lower average fluorescence of the $|\pm1\rangle$ spin transition and can be optically detected and readout. Sweeping the applied microwave frequency leads to the ESR spectra in Fig. 2(b), from which $v_\pm$ can be determined.

According to the energy levels of the diamond NV centers, a microwave sweep signal with a center frequency of 2.87 GHz is required. The optical filter is needed to select the fluorescence and reject the 532 nm green laser. The photon detector receives the fluorescence signals. In our work, all these functional modules are integrated using the HMIC technique. The overall system schematic is illustrated in Fig. 2(d). With the green laser pumping, the integrated microwave circuit manipulates the qubit resonance of the NV centers and collects the fluorescence signals, respectively. This is followed by signal analysis and magnetometer readout.
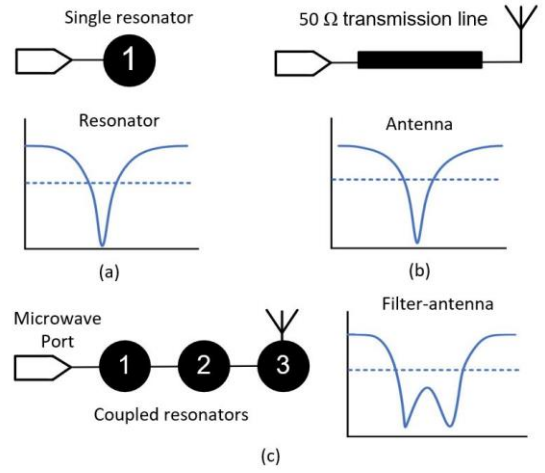

Fig. 3 Microwave coupling topologies and reflection response which drive the diamond NV centers. (a) Single resonator. (b) Antenna with 50 Ω transmission line. (c) Filtering antenna.

B. Filtering Antenna Integrated VCO Synthesis for Improved Sensitivity

In traditional solutions, loop antenna [24], [27], ring resonator [28], microstrip transmission line [26], or coplanar waveguide [29] are often employed to excite the NV centers. These microwave delivery techniques often cascade the single resonator and antenna by 50 Ω transmission line (see Fig. 3(a) and (b)). However, these components suffer from low coupling efficiency over a wide bandwidth. Since the ESR resonance contrast is proportional to the power of the microwave excitation, narrow bandwidth and low power transfer efficiency can degrade the sensor's performance. In this work, the multiple resonators-based filtering antenna is proposed to replace the single resonator and the narrow band antenna. As illustrated in Fig. 3(c), a radiant resonator is coupled to the end of the filter, providing a uniform broadband filtering response and gain.

Next, let us discuss the sensitivity contribution from the filtering antenna. In the ODMR-based magnetic field measurement, the sensitivity η_{th} of the NV-based DC magnetic field sensor is given by [30]

$$\eta_{th} = P_F \frac{1}{\gamma_e} \frac{\Delta v \sqrt{t_m}}{\alpha \sqrt{\beta}} \tag{2}$$

where α is the resonance contrast, β is the number of photons collected per measurement, Δv is resonance linewidth, and t_m measurement duration. P_F is a scalar factor relying on the NV resonance types, and $P_F \approx 0.70$ for a Gaussian lineshape, $P_F \approx 0.77$ for a Lorentzian lineshape. Note that these parameters are not independent variables. The resonance contrast α can be increased by increasing the power of the microwave excitation at the expense of increased the linewidth Δv due to power broadening. Likewise, the linewidth Δv may be decreased (down to a limit defined by the NV spin dephasing time T_2^*) by lowering the laser excitation power to reduce power broadening; however, doing so decreases the number of photons collected per measurement β. Fortunately, these parameters can be optimized to obtain the optimum DC sensitivity [31], yielding

$$\eta_{th} \propto P_F \frac{1}{\gamma_e} \frac{1}{\alpha \sqrt{\beta T_2^*}} \tag{3}$$

In the system, the photodetector and the laser excitation power are constant, and T_2^* and β remain unchanged. Thus, since the α is in direct proportion to the microwave power in the unsaturated range [30], a transfer function $H(j\omega)$ can be introduced to evaluate the microwave power transfer from the VCO to the NV centers. ω is the frequency variable in rad/s. Therefore, the average sensitivity is proportional to microwave power transfer characterized by $H(j\omega)$, given by

$$\eta_{th} \propto \frac{BW}{\int_{\omega_{low\_cutoff}}^{\omega_{high\_cutoff}} H(j\omega)} \tag{4}$$

where BW is the bandwidth of the filtering antenna; ω_{low_cutoff} and ω_{high_cutoff} are the low and high cut-off frequencies of BW. Note that the magnetic sensitivity relationship (3) and (4) are validated only in pulsed-ESR techniques which is the method we used in our experiment. According to (4), the magnetic sensitivity can be improved by optimizing the transfer function $H(j\omega)$, which can be synthesized by the integrated filtering antenna.

Another benefit of the integrated filter elements is the reduced phase noise. The integrated filter structure can effectively reduce phase noise of oscillators. The theory has been well proved in [32], [33]. The measured phase noise of the VCOs will be presented in Section IV. Here, the effect of the VCO phase noise on the sensitivity is estimated.

Referring to the Leeson's oscillator model [32], the output oscillation spectrum of the VCO can be expressed as

$$S_\phi(\delta\omega) = S_\theta \left[1 + \left(\frac{\omega_0}{2Q_S \delta\omega}\right)\right] \tag{5}$$

where $\delta\omega$ is the offset frequency from the oscillation frequency ω_0, S_θ is the additive noise component, and Q_S is the spectrum-based quality factor, which dominates the oscillation spectrum. The offset frequency $\delta\omega$ around the operating frequency (ω_0) is related to the phase noise by [25]

$$\delta\omega = \frac{d\phi_n(t)}{dt} \tag{6}$$

ϕ_n is the phase noise of the microwave frequency of the VCO. The estimated magnetic sensitivity S_m due to phase noise converted from the VCO can be estimated by [25]

$$S_m \approx \frac{\phi_n}{\gamma_e} \tag{7}$$

The measured phase noise of the VCO with a filtering antenna achieves ~14 dBc/Hz lower than the VCO with a single resonator. The improvement of the magnetic sensitivity calculated from (7) is ~4.78 pT/Hz$^{1/2}$.

III. THE CIRCUIT DESIGN AND PHYSICAL CONSTRUCTION OF THE SENSOR

A. Design of the VCO Integrated with Filtering Antenna

The lumped circuit schematic of the microwave source is shown in Fig. 4(a). The terminal network we used is a three
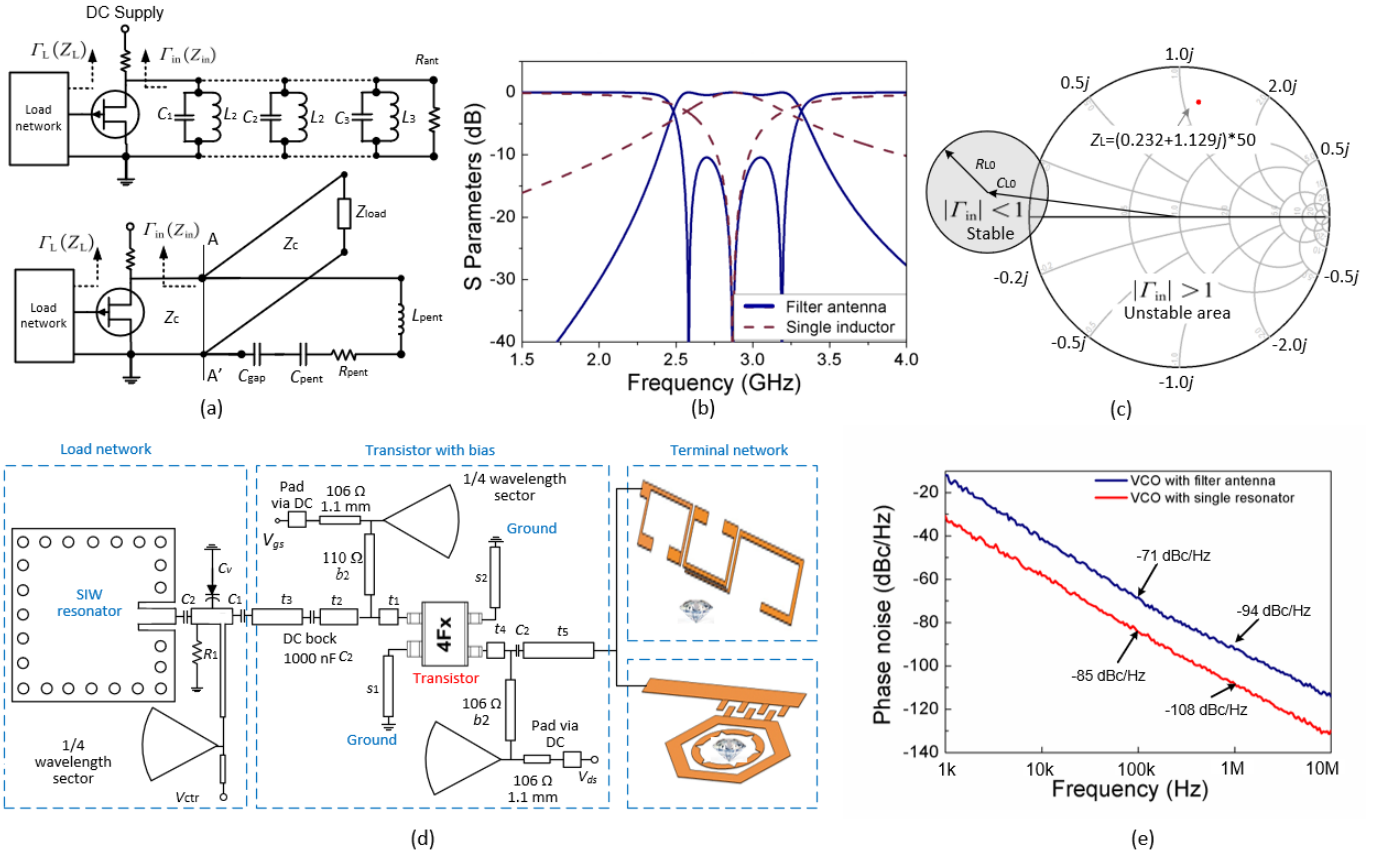

Fig. 4 (a) Lumped circuits of the VCO integrated with a filter-antenna and a single resonator. (b) Transmission responses of the multiple resonators-based filter and a single resonator. (c) Output stability circle of the GaAs transistor with bias. (d) Schematic circuit representation of the VCO. (e) Measured phase noise.

resonators-based filtering antenna. To make a comparison, the VCO with a single hexagon loop resonator is also designed. All other parts of the circuit are the same. In Fig. 4(a), L_{pent} and C_{pent} are the serial inductor and capacitor, forming a resonator. R_{pent} is the load of the resonator. They are determined by the hexagonal resonator and the diamond sample itself. C_{gap} is determined by the narrow gap between the resonator and the transmission line. Z_{load} is the load impedance of the transmission line. The filter antenna is formed by three resonators (L_i and C_i, $i= 1$ to 3). R_{ant} represents the radiate resistor. All the parameters of equivalent circuits can be determined according to the desired circuit responses. These circuits can also be transformed into microstrip structures using the classic microwave equivalent circuit topologies [35]. Then, the transfer function $H(j\omega)$ can be obtained once the circuits are determined. The transfer function $H(j\omega)$ corresponding to the S-parameters of the filter, given by [35]

$$H(j\omega) = S_{21} \tag{8}$$

Here, we use a 3rd order Chebyshev filtering response with a center frequency of 2.87 GHz, 10 dB return loss and 25% fractional bandwidth (*FBW*). The coupling matrix of the filter can be calculated according to [36], given by

$$[m] = \begin{bmatrix} 0 & 0.8148 & 0 & 0 & 0 \\ 0.8148 & 0 & 0.7716 & 0 & 0 \\ 0 & 0.7716 & 0 & 0.7716 & 0 \\ 0 & 0 & 0.7716 & 0 & 0.8148 \\ 0 & 0 & 0 & 0.8148 & 0 \end{bmatrix} \tag{9}$$

The resultant S-parameters are plotted in Fig. 4(b). Note that the filter response presents a broader and more uniform passband than the single loop resonator.

The next step is to determine the physical construction of transistor VCO and the load networks. The transistor output stability circle and circuit schematic of the VCO are shown in Fig. 4(c) and (d). A common source structure is used. The transistor is the ATF-54143 GaAs pHEMT [37]. The grounded microstrip lines s_1 and s_2 are tuned to ensure that S_{11} and S_{22} of the transistor are above zero. Note that the gate and drain of the transistor are assumed to be the input and output. R_{L0} and C_{L0} are the radius and center of $|\Gamma_{in}|=1$ circle. Recall the reflection coefficient of the transistor $S_{11} > 0$. The inside area of the stability circle is stable. The reflection coefficient Γ_T is located around 50 Ω on the Smith Chart in Fig. 4(d). Then, the reflection coefficient seen from the transistor gate Γ_{in} can be calculated by [35]

$$\Gamma_{in} = S_{11} + \frac{S_{12}S_{21}\Gamma_T}{1 - S_{22}\Gamma_T} \tag{10}$$

Then the load impedance $Z_L = R_L + jX_L$ is determined to fulfil

$$\Gamma_{in}\Gamma_T = 1 \tag{11}$$

For practical consideration, we choose

$$R_L = -\frac{R_{in}}{3} \tag{12}$$

$$X_L = -X_{in} \tag{13}$$
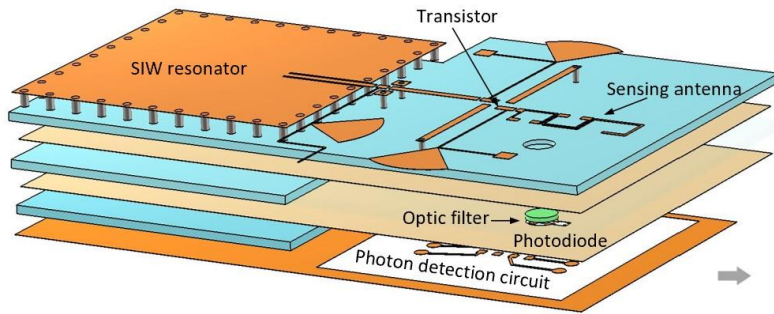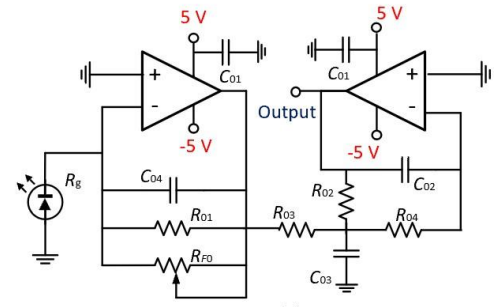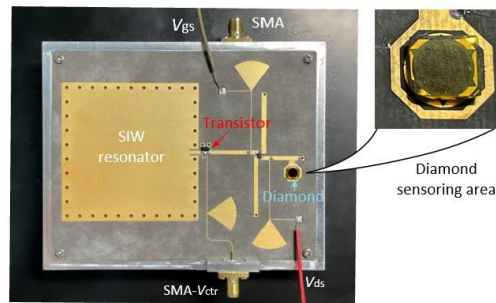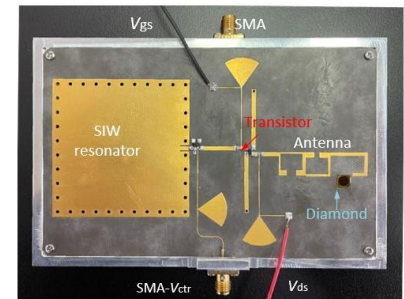
Fig. 5. (a) Three-dimensional diagram of the circuit stack view. (b) Sectional view. (c) The photodetection and the amplifier circuit. (d) Photos of manufactured HMICs employing VCO integrated with single resonator and (d) VCO integrated with filtering antenna.

TABLE II
GEOMETRIES OF THE VOC HMIC

Parameters	Values	Parameters	Values
t_1	2.80 mm	b_1	23.12 mm
t_2	0.50 mm	b_2	23.20 mm
t_3	15.53 mm	c_1	4 pF
t_4	3.30 mm	c_2	1000 pF
t_5	6.7 0mm	c_L	100 pF
t_6	2.90 mm	R_0	50 Ω
s_1	23.66 mm	R_1	110 Ω
s_2	23.56 mm	θ	75 deg
s_3	22.86 mm	a	51.80 mm

TABLE III
COMPONENTS VALUES OF THE PHOTON DETECTOR CIRCUIT

Capacitors	Values	Resistors	Values
C_{01}	100 nF	R_{01}	1 MΩ
C_{02}	1.2 nF	R_{02}	47 kΩ
C_{03}	270 nF	R_{03}	470 Ω
C_{04}	0.2 pF	R_{04}	430 Ω

Fig. 6 Response of the amplifier and the spectral responsivity of the PIN silicon photodiode.
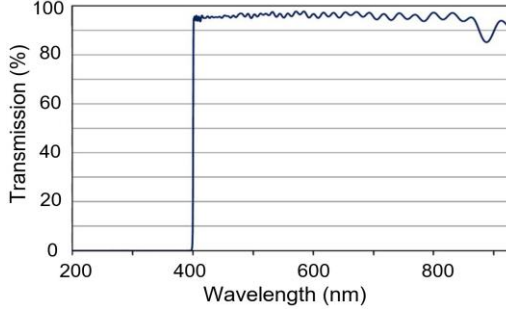
Fig. 7 Response of the 600 nm long-pass optic filter.
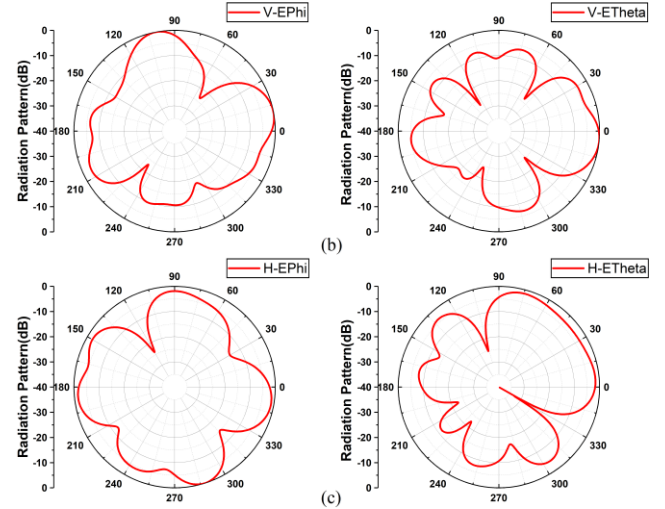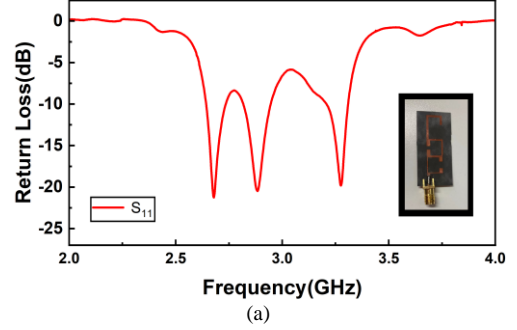
Fig. 8. (a) Measured return loss of the filtering antenna. Measured radiation pattern of filtering antenna at zero-field splitting frequency 2.87 GHz with (b) XOY pattern and (c) YOZ pattern.
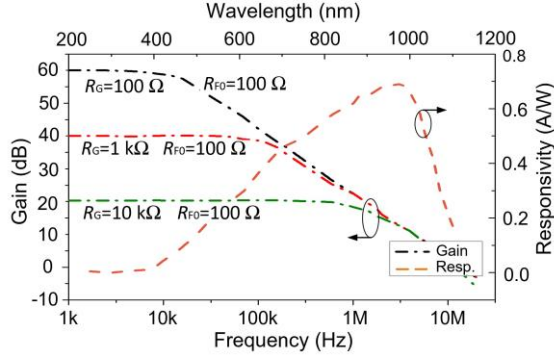
The S-parameters of the transistor with bias can be obtained from the S2P touchstone file of the transistor and its EM simulation using ADS. These are given in Table I. Γ_T can also be obtained via EM simulation, given by $-0.4096 - 0.3804j$. According to (10), Γ_{in} can be calculated to be $-1.1092 + 0.995j$. Referring to (12) and (13), the load impedance can be determined to be $Z_L = 50·(0.232 + 1.129j)$ Ω. R_1 and C_1 are the load resistor and capacitor, while impedance seen from the gate of the transistor can be adjusted through the transmission line t_3. The abrupt junction tuning varactor C_V is used for frequency tuning of the oscillator. The modulated signals can be exerted via the microstrip line s_3. The geometries of the VCO construction are given in Table II.

Due to the introduced filtering elements, the noise figure is reduced. The measured results are shown in Fig. 4(e). The VCO with the filter-antenna presents a lower phase noise (-108 dBc/Hz at 1 MHz offset frequency) than the VCO with the single resonator (-94 dBc/Hz at 1 MHz offset frequency). This contributes to the overall sensitivity improvement as we discussed in Section II.

B. Co-design of the Optic Filter, Photon Detection and Amplifier Circuits

Now let us introduce the co-designed optic filter and fluorescence detection circuits. The optical modules are also designed using multiple layer HMIC technique. Fig. 5(a) illustrates the three-dimensional circuit stack of the architecture. It contains three stacked substrates and four circuit layers. The microwave circuit is located on the first layer; the photon detection and amplifier circuit are on the third and fourth layers. The optic filter is sandwiched between the third and fourth layers. Fig. 5(b) illustrates the sectional view of the substrate stack. The fluorescence detection circuit (see Fig. 5(c)) is located at the bottom layer, and it includes a photodiode and an amplifier. The HMIC was fabricated using the RT/5880 and FR4 substrate stack, corresponding to the relative dielectric constant ε_r of 2.2 and 4.4, respectively. The aluminium housing was made to fix the PCB board. Fig. 5(d) and (e) are the photos of the fabricated VCOs.

In the fluorescence detection circuit, an enhanced PIN silicon photodiode PDB-C160SM is used [38]. The spectral response of the photodiode is shown in Fig. 6, indicating the responsivity is 0.37 A/W at the wavelength of 650 nm. The amplifier is realized by a low noise JFET ISL28210 [39]. A variable resistor feedback R_{F0} is used to adjust the closed-loop gain and the corresponding bandwidth. R_g is the equivalent resistance of the photodiode. Referring Fig. 5(c), the closed loop gain of the amplifier can be calculated by

$$Gain \approx 20 \cdot \log \frac{R_{01} R_{02} R_{F0}}{R_{03} R_g (R_{01} + R_{F0})} \tag{14}$$

The circuit the response of the amplifier is shown in Fig. 6. The parameters of the bias circuit are given in Table III. The 600 nm optic long-pass filter [40] is sandwiched by the 2nd and the 3rd layers, where the transmission response is shown in Fig. 7. The average transmission efficiency is over 91% from 610 nm to 1650 nm and < 0.01% from 200 nm to 588 nm.

To investigate the microwave circuit part, the antenna was fabricated and measured independently. The measured return loss (S_{11}) of the filter antenna is illustrated in Fig. 8(a). The S_{11} is around -10 dB from 2.6 GHz to 3.3 GHz, corresponding to a wide bandwidth that allows for magnetic field sensing range. The measured radiation pattern at zero-field splitting frequency 2.87 GHz is shown in Fig. 8(c) and (d).

IV. EXPERIMENTS AND RESULTS

A. Experiment System Setup

The diamond was grown by a microwave plasma chemical vapor deposition (MPCVD) method using a high-pressure and high-temperature Ib-type diamond as the substrate. CH_4 and H_2 were used as the precursors for the growth of the diamond; the flow rates of CH_4 and H_2 are 10 and 190 sccm respectively. During the growth process, the chamber pressure was kept at 350 mbar; the microwave power was set to 3000 W; the substrate temperature was maintained at 950 ºC. After the synthesis, the diamond was cut off from the substrate and polished mechanically. Last, the diamond was immersed in aqua regia to remove any adsorbate introduced during the polishing process.

The experiment setup is shown in Fig. 9(a). A 532 nm green light laser is placed, together with the lens and mirrors to form the light beam. The power of the laser can be adjusted to obtain a good fluorescence. In our example, the laser power is about 2 mW. With the help of an acoustic optical modulator (AOM), the continuous laser is converted to a light pulse initiating the spin state of the NV centers. The VCO is modulated by a signal generator to produce sweeping waveforms. The LabVIEW virtual instrument and signal analyzer are used for data acquisition. A synchronizer is set up to synchronize the data acquirer and the laser pulse.

B. Measurement and Results

In the magnetic field sensing system, a three-axis coil is employed to offer the static magnetic field. The resultant ODMR spectrum is shown in Fig. 9(b), where the Zeeman splitting can be observed. The spectrum splits eight discrete resonance peaks under the external static magnetic field. The bias components of the magnetic field can be determined by the
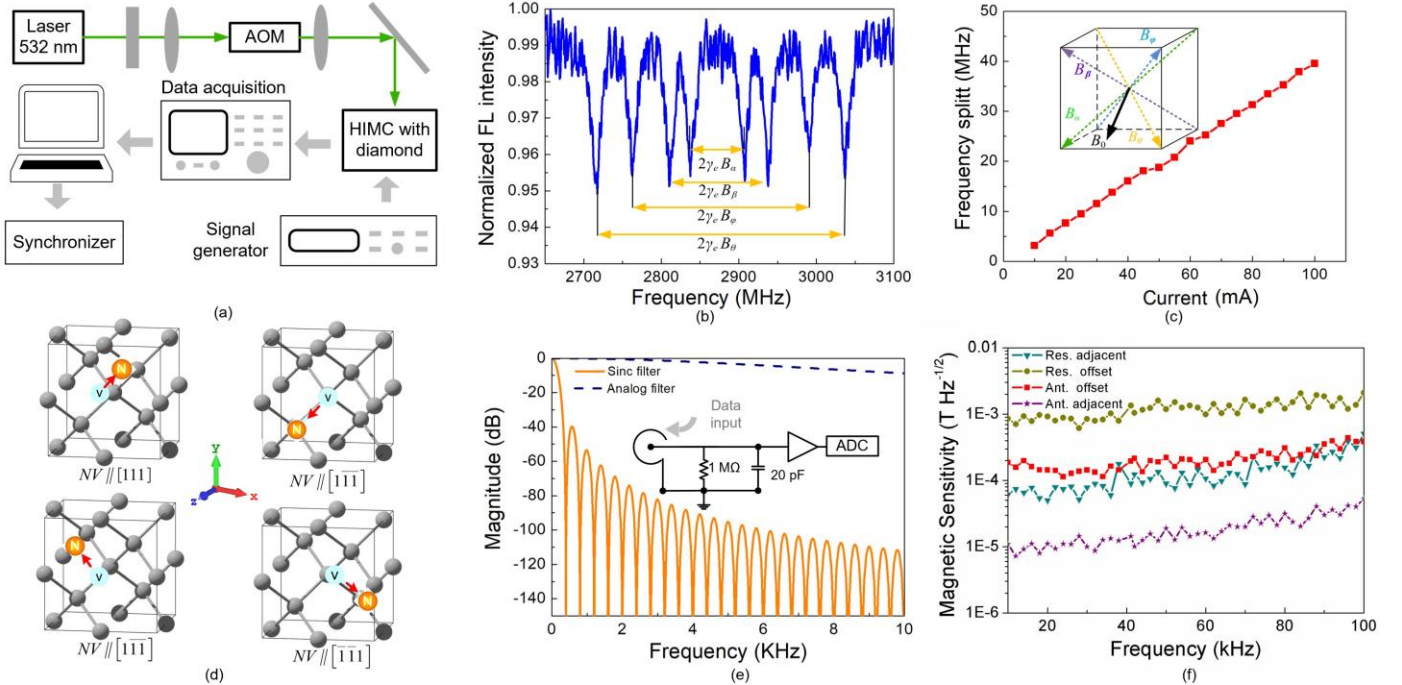

Fig. 9 (a) Schematic of the experiment setup. Connection of the synchronizer is omitted. (b) Measured ESR spectrum using the HMIC and diamond assembly. (c) Frequency shift versus applied current in the coils. (d) Four orientations of the NV centers. Red arrows represent the NV electronic spin. (e) Circuit diagram of the digitizer and filter response. (f) Measured noise density.

TABLE IV
COMPARISON OF NV-BASED MAGNETIC FIELD SENSORS USING MICROWAVE ICS

Ref.	Phase noise	VCO Tuning range	Process & Technol.	Microwave delivery	Sensitivity	Dynamic range
[24]	−90 dBc/Hz@1.5 kHz	2.6-3.1 GHz	CMOS & PCB	Loop inductor	32 µT/Hz$^{1/2}$	*24.77 dB
[25]	−88 dBc/Hz@3 kHz	N/A	CMOS & PCB	Wire array	245 nT/Hz$^{1/2}$	N/A
This work	−91 dBc/Hz@100 kHz	2.67-3.12 GHz	GaAs & PCB	Ring resonator	107 µT/Hz$^{1/2}$	17.88 dB
	−105dBc/Hz@100kHz	2.58-3.31 GHz	GaAs & PCB	Filtering antenna	8.52 µT/Hz$^{1/2}$	32.73 dB

N/A: This specification is not given in the reference. *This specification is calculated according to the related parameters given in the reference.

frequency shift. The eight resonance peaks are symmetrically distributed on both sides of the zero-field splitting (ZFS) frequency. This is because the NV axis may be oriented along with one of the four possible tetrahedral directions, i.e. [111], [$\bar{1}$11], [1$\bar{1}$1], [$\bar{1}\bar{1}$1]. Note that as the experiment is carried out at constant temperature, the ZFS frequency is 2.87 GHz. The magnetic field components corresponding to Δf_α, Δf_β, Δf_φ, and Δf_θ can be calculated by

$$B_i = \frac{\Delta f_i}{\gamma_e} \ (i = \alpha, \beta, \varphi, \text{ and } \theta) \quad (15)$$

We assume the biases along the four directions of the NV axis are B_α, B_β, B_φ, and B_θ, respectively (see Fig. 9(b) and (c)). The frequency shift corresponding to electronic spin resonance between $|m_s = \pm1\rangle$ is proportional to the projection of the magnetic field B_0 along the NV symmetry axis. Fig. 9(c) presents the linear relationship between the frequency split Δf_α and the applied coil current. The four NV axis structures are illustrated in Fig. 9(d), where four directions are possible by flipping the nitrogen atom and vacancy in each configuration. By mapping the bias of the static magnetic field along the four NV-axis to a Cartesian coordinate, the magnetic field vector can be obtained.

The sensitivity of the device which evaluates the minimum detectable magnetic field is estimated by

$$S = \frac{\sigma_0}{ENBW} \quad (16)$$

where σ_0 is the noise in the B_i measurements and $ENBW$ is the equivalent noise bandwidth of the data acquisition. σ_0 is from the measurement and the $ENBW$ can be obtained according to the parameters of the acquisition. The $ENBW$ typically depends on the smallest cutoff frequency of the filters in the system. Conventional digitizer comprises a two-stage system including an anti-aliasing filter and an analog-to-digital (ADC) module integrated with a sinc filter. The NI-9775 digitizer from National Instrument was used. As illustrated in Fig. 9(f), a single-pole resistor-capacitor (RC) anti-aliasing filter is before the digital converter. The resistor and capacitor are given by 1 MΩ and 20 pF. The analog anti-aliasing filter response (dashed line) and the sinc filter response (solid line) are given in Fig. 9(e). The corresponding cutoff frequency is 5.1 kHz and 1.1 Hz, respectively. Note that the bandwidth of the anti-aliasing filter is much wider than the sinc filter. Thus, the $ENBW$ can be approximately given by

$$ENBW \approx f_{\text{ADC\_cutoff}} \quad (17)$$

Substitute (17) into (16), the sensitivity of the magnetic field sensor can be obtained.

Fig. 9(f) illustrates the measured sensitivity versus the modulated frequency from 1 kHz to 100 kHz. To make a comparison, the VCO with the single resonator and the filtering antenna are used in the experiment, respectively. Two groups of measurement are made. First, the diamond is placed 1.5 mm offset the antenna and the resonator, respectively. As illustrated in Fig. 9(f), at 60 kHz frequency, the VCO with filtering antenna achieves a sensitivity of 205.4 µT/Hz$^{1/2}$, whereas the single resonator VCO achieves 994.1 µT/Hz$^{1/2}$. Second, the diamond is on the surface of the resonator and the antenna, respectively. The measured sensitivity of the resonator device is 107 µT/Hz$^{1/2}$ and the sensitivity of the filtering antenna device is 8.5 µT/Hz$^{1/2}$. Both experiment results demonstrate our developed VCO integrated with a filtering antenna can achieve an improved sensitivity of the NV-based magnetic field sensor. Note that when the diamond is closer to the device, the sensitivity is increased. This is due to a stronger microwave field at the surface of the microwave circuits.

The measured tuning range of the VCO with filtering antenna and single resonator is 2.58-3.31 GHz and 2.67-3.13 GHz, respectively. Considering the $ENBW$ in (16), minimum detectable magnetic field are 8.5 µT (VCO with filtering antenna) and 117.7 µT (VCO with a resonator). The maximum detectable magnetic fields, at which the sensor begins to show nonlinearity, are given by 15.93 mT (VCO with filtering antenna) and 7.23 mT (VCO with a resonator). The corresponding dynamic range of VCO with filtering antenna and single resonator sensor is 8.5 µT/Hz$^{1/2}$ to 14.3 mT/Hz$^{1/2}$, respectively. a resonator). Thus, the corresponding dynamic range of sensors can be obtained by the ratio of maximum and minimum detectable magnetic field, given by 32.73 dB (VCO with filtering antenna) and 17.88 dB (VCO with a resonator), respectively.

A comparison of NV-based magnetic field sensors using other microwave ICs is presented in Table IV. We achieve about ×4 times sensitivity improvement than [24], and 7.96 dB dynamic range improvement than [24]. Compared to the single resonator VCO, our filtering antenna integrated with VCO realized improved performance of the magnetic sensor in terms of sensitivity and dynamic range. Note that magnetic sensitivity calculated from (7) is ~4.78 pT/Hz$^{1/2}$, which is much smaller than the measured results from (16) and (17), which indicates that the oscillator's phase noise does not limit the sensitivity of the system.

Other variables factors that affect the sensitivity include the laser, optic filter, photodiode, and the diamond sample, which are discussed as follows. According to [25], the sensitivity is inversely proportional to the SNR of the sensor,

$$S \propto \frac{1}{\text{SNR}} = \frac{\sigma_i \cdot \Delta v}{\gamma_e \cdot I_r} \qquad (18)$$

Here, σ_i is the total noise current density (unit: A/Hz$^{1/2}$), I_r is the photo-current of the fluorescence signal. In the system, the linewidth Δv can be optimized by adjusting the laser power and the modulated frequency to reduce power broadening. In the measurement, the linewidth of the ODMR can be optimized to 10 MHz. The noise is determined by the shot noise of either the green excitation and the red fluorescence [25]

$$\sigma_i = \sqrt{2 \cdot q \cdot (I_g + I_r)} \qquad (19)$$

In (18), q is the electronic charge; I_r and I_g are the photo-currents from the red fluorescence signal and the unfiltered green laser. The photo-currents I_g can be estimated by

$$I_g = P_g . R_{\text{PD}} \cdot \eta_g \qquad (20)$$

Here, P_g is the input optical power. R_{PD} is the photodiode responsivity, which is from 0.02 A/W to 0.69 A/W over 10 K to 10 M frequency, as shown in Fig. 6. η_g is the green rejection of the optical filter, and is more the 99.9% from 200 nm to 588 nm. The value of I_r is proportional to the density (ρ_{nv}) of NV centers in the diamond and sensing area of the photodiode. According to (18)-(20), the sensitivity can be determined by the laser, photodiode, optic filter, as well as the diamond itself. Note that these parameters are not independent of each other, and the optimum magnetic sensitivity can be achieved through global optimization of these parameters.

V. CONCLUSIONS

In this paper, the NV-based quantum magnetic sensor using the HMIC technique is demonstrated. Microwave sweeping, optic filtering, and photon detection modules are integrated into a stacked substrate to form a compact entity. Thus, conventional NV-based magnetic metrologies, which rely on costly and bulky microwave and optic instruments, can be partly simplified and optimized through this HMIC and diamond assembly. Conventional microwave delivery components such as single resonator, microstrip transmission line, loop antenna, or coplanar waveguide are replaced by VCO integrated filtering antenna. This can provide a more uniform, efficient and lower phase noise coupling microwave field to driving the NV centers, leading to improved sensitivity. The VCO integrated with filtering antenna may also provide a possibility of non-contact sensing of diamond NV quantum system. Although the example is demonstrated as a magnetometer, the approach is general and enables us to develop on-chip integrated circuits (ICs) and devices dealing with a wide range of solid-state-based quantum systems.

There are some limitations in this work. In our design, only a sweeping microwave source is implemented. Additional circuits may be integrated, for instance, a phase shift network is expected to enable the lock-in technique which may improve the SNR and sensitivity. The laser may also be integrated within the device to form a more compact architecture.

Besides the NV centers in diamond, many other quantum solid-state systems operate in the microwave frequency regime, usually ranging from S to K band [41], [42]. The hybrid microwave integrated circuits introduced in this work or other monolithic microwave integrated circuits (MMIC) allow us to

envision potential low-cost, flexible and practical quantum-based measurements, sensing and computing applications.

References

[1] E. Alipieva, S. V. Gateva and E. Taskova, "Potential of the single-frequency CPT resonances for magnetic field measurement," *IEEE Trans. Instrum. Meas*, vol. 54, no. 2, pp. 738-741, Apr. 2005

[2] C. Affolderbach, G. Du, T. Bandi, A. Horsley, P. Treutlein and G. Mileti, "Imaging microwave and DC magnetic fields in a vapor-cell Rb atomic clock," *IEEE Trans. Instrum. Meas*, vol. 64, no. 12, pp. 3629-3637, Dec. 2015

[3] A. H. Khawaja, Q. Huang and Y. Chen, "A novel method for wide range electric current measurement in gas-insulated switchgears with shielded magnetic measurements," *IEEE Trans. Instrum. Meas*, vol. 68, no. 12, pp. 4712-4722, Dec. 2019.

[4] Y. Ying, Y. Zhao, R. Lv and H. Hu, "Magnetic field measurement using surface plasmon resonance sensing technology combined with magnetic fluid photonic crystal," *IEEE Trans. Instrum. Meas*, vol. 65, no. 1, pp. 170-176, Jan. 2016.

[5] A. M. Nazar, P. Jiao, Q. Zhang, K. -J. I. Egbe and A. H. Alavi, "A new structural health monitoring approach based on smartphone measurements of magnetic field intensity," *IEEE Instrum. Meas.Magaz.*, vol. 24, no. 4, pp. 49-58, Jun. 2021.

[6] A. Zhukov, M. Ipatov, P. Corte-Leon, J. M. Blanco, L. González-Legarreta and V. Zhukova, "Routes for optimization of giant magnetoimpedance effect in magnetic microwires," *IEEE Instrum. Meas. Magaz.*, vol. 23, no. 1, pp. 56-63, Feb. 2020

[7] J. Wu and B. N. Li, "Development of a magnetoinductive lens for magnetic resonance imaging," *IEEE Instrum. Meas. Magaz.*, vol. 20, no. 6, pp. 56-60, Dec. 2017.

[8] X. Ding and S. Ren, "Accuracy analysis of sensing coils in 2-D magnetic properties measurement," *IEEE Trans. Magnetics*, vol. 54, no. 11, pp. 1-5, Nov. 2018.

[9] H. J. Mamin *et al.*, "Nanoscale nuclear magnetic resonance with a nitrogen-vacancy pin sensor" *Science*, vol. 339, no. 6119, pp. 557-560, Feb. 2013.

[10] G. Kucsko *et al.*, "Nanometre-scale thermometry in a living cell," *Nature*, vol. 500, pp. 54–58, Jun. 2013.

[11] T. Staudacher *et al.*, "Nuclear magnetic resonance spectroscopy on a (5-nanometer)^3 sample volume" *Science*, vol. 339, no. 6119, pp. 561-563, Feb. 2013.

[12] D. A. Broadway *et al.*, "Spatial mapping of band bending in semiconductor devices using in situ quantum sensors," *Nat. Electron.*, vol. 1, pp. 502–507, Sept. 2018.

[13] F. Dolde *et al.*, "Electric-field sensing using single diamond spins," *Nat. Phys.*, vol. 7, pp. 459–463, Apr., 2011.

[14] K. Jensen *et al.*, "Cavity-enhanced room-temperature magnetometry using absorption by nitrogen-vacancy centers in diamond," *Phys. Rev. Lett.*, vol. 112, pp. 16-25, Apr., 2014.

[15] J. M. Boss, K. Cujia, J. Zopes, and C. L. Degen, "Quantum sensing with arbitrary frequency resolution," *Science*, vol. 356, no. 6340 pp. 837–840, May 2017.

[16] C. Affolderbach, G. Du, T. Bandi, A. Horsley, P. Treutlein and G. Mileti, "Imaging microwave and DC magnetic fields in a vapor-cell rb atomic clock," *IEEE Trans. Instrum. Meas.*, vol. 64, no. 12, pp. 3629-3637, Dec. 2015, doi: 10.1109/TIM.2015.2444261.

[17] X. Liu, Z. Jiang, J. Qu, D. Hou and F. Sun, "Rabi resonances in buffer-gas-filled cs-vapor cells for SI-traceable microwave magnetic field detection," *IEEE Trans. Instrum. Meas.*, vol. 69, no. 4, pp. 1302-1307, Apr. 2020.

[18] M. Zhu, M. Toda and T. Ono, "Fabrication of an assembled scanning probe with nitrogen vacancy centers in diamond particle," *IEEE Trans. Nanotechnol.*, vol. 16, no. 4, pp. 545-550, Jul. 2017.

[19] A. Horsley et al, "Microwave device characterization using a widefield diamond microscope," *Physic. Rev. Appl.*, vol., no.4, 2018.

[20] G. Chen, B. Gu, W. He, Z. Guo and G. Du, "Vectorial near-field characterization of microwave device by using micro diamond based on tapered fiber," *IEEE Jour. Quantum Electron.*, vol. 56, no. 3, pp. 1-6, Jun. 2020.

[21] B. Yang *et al.*, "Using diamond quantum magnetometer to characterize near-field distribution of patch antenna," *IEEE Trans. Microw. Theory Techn.*, vol. 67, no. 6, pp. 2451-2460, Jun. 2019.

[22] B. Yang, Y. Dong, Z. Hu, G. Liu, Y. Wang and G. Du, "Noninvasive imaging method of microwave near field based on solid-state quantum sensing," *IEEE Trans. Microw. Theory Techn.*, vol. 66, no. 5, pp. 2276-2283, May 2018.

[23] Z. Hu, B. Yang, M. Dong, Y. Liu, Y. Wang and G. Du, "Optical sensing of broadband RF magnetic field using a micrometer-sized diamond," *IEEE Trans. Magnetics*, vol. 55, no. 3, pp. 1-4, Mar. 2019.

[24] D. Kim, M. I. Ibrahim, C. Foy *et al.*, "A CMOS-integrated quantum sensor based on nitrogen-vacancy centres," *Nat. Electron.*, vol. 2, no. 7, pp. 284-289. 2019.

[25] M. I. Ibrahim, C. Foy, D. R. Englund, R. Han, "High-scalability CMOS quantum magnetometer with spin-state excitation and detection of diamond color centers," *IEEE Jour. Solid*-State Circ., vol. 56, no. 3, pp. 1001-1014, Mar. 2021.

[26] N. D. Lai, D. Zheng, F. Jelezko, F. Treussart, J. F. Roch, "Influence of a static magnetic field on the photoluminescence of an ensemble of nitrogen-vacancy color centers in a diamond single crystal," *Appl. Phys. Lett.*, vol. 95, 133101, 2009.

[27] P. L. Stanwix, *et al.*, "R. L. Coherence of nitrogen-vacancy electronic spin ensembles in diamond," *Phys. Rev. B*, vol. 82, 201201, 2010.

[28] K. Bayat, L. Choy, M. F. Baroughi *et al.*, "Efficient, uniform, and large area microwave magnetic coupling to NV centers in diamond using double split-ring resonators," *Nano Lett.*, vol. 14, no. 3, pp. 1208-1213, 2014.

[29] G. De Lange *et al.*, "Controlling the quantum dynamcis of a mesoscopic spin bath in diamond," *Sci. Rep.*, vol. 2, 382, 2012.

[30] L. M. Pham, "Magnetic field sensing with nitrogen-vacancy color centers in diamond," Ph.D. dissertation, Harvard Univ., Cambridge, MA, USA, 2013.

[31] A. Dréau *et al*, "Avoiding power broadening in optically detected magnetic resonance of single NV defects for enhanced DC-magnetic field sensitivity," *Phys. Rev. B*, vol. 84, 195204, 2011.

[32] J. Choi, M. Nick and A. Mortazawi, "Low phase-noise planar oscillators employing elliptic-response bandpass filters," *IEEE Trans. Microw. Theory Techn.*, vol. 57, no. 8, pp. 1959-1965, Aug. 2009.

[33] Y. Gao *et al.*, "Coupling matrix-based co-design of filter-oscillators," *IEEE Microw. Wirel. Compon. Lett.*, early access, doi: 10.1109/LMWC.2022.3146181.

[34] C. Tseng and C. Chang, "Design of low phase-noise microwave oscillator and wideband VCO based on microstrip combline pandpass filters," *IEEE Trans. Microw. Theory Techn.*, vol. 60, no. 10, pp. 3151-3160, Oct. 2012.

[35] D. Pozar, Microwave engineering. Hoboken, NJ: Wiley, 2012.

[36] J. S. Hong and M. J. Lancaster, *Microstrip Filters for RF/Microwave Applications*. New York, NY, USA: Wiley, 2001.

[37] Agilent Technologies, Inc., CA., USA, Available: www.agilent.com.

[38] Advanced Photonix Corp., CA., Available: www.advancedphotonix.com.

[39] Intersil Corp., CA., Available: www.intersil.com.

[40] Edmund Optics Inc., NJ., USA, Available: www.edmundoptics.com.

[41] J. C. Bardin, D. Sank, O. Naaman and E. Jeffrey, "Quantum computing: an introduction for microwave engineers," *IEEE Microw. Magaz.*, vol. 21, no. 8, pp. 24-44, Aug. 2020.

[42] D. Ristè, S. Fallek, B. Donovan and T. A. Ohki, "Microwave techniques for quantum computers: state-of-the-art control systems for quantum processors," *IEEE Microw. Magaz.*, vol. 21, no. 8, pp. 60-71, Aug. 2020.